ACS NANO

www.acsnano.org

ARTICLE

Two-Dimensional Tantalum Carbo-Selenide for Hydrogen Evolution

Elham Loni, Ahmad Majed, Shengjie Zhang, Hari H. S. Thangavelu, Chaochao Dun, Anika Tabassum, Karamullah Eisawi, Jeffrey J. Urban, Per O. Å. Persson, Matthew M. Montemore, and Michael Naguib*

Cite This: *ACS Nano* 2025, 19, 3185−3196

Read Online

ACCESS | Metrics & More | Article Recommendations | Supporting Information

ABSTRACT: **Herein, we report the synthesis of two-dimensional Ta_2Se_2C (2D-Ta_2Se_2C) nanosheets using electrochemical lithiation in multilayer Ta_2Se_2C followed by sonication in deionized water. Multilayer Ta_2Se_2C was obtained via solid-state synthesis of $Fe_xTa_2Se_2C$ followed by chemical etching of Fe. 2D-Ta_2Se_2C exhibited promising electrocatalytic activity for the hydrogen evolution reaction from water compared to multilayer Ta_2Se_2C and 2D-$TaSe_2$. 2D-Ta_2Se_2C showed an overpotential at 10 mA·cm^{-2} (η_{10}) of 264 mV, a Tafel slope of 91 mV·dec^{-1}, and an electrochemically active surface area of 17.61 m_{ECSA}^{2}·$g_{catalyst}^{-1}$. The high performance could be attributed to the large surface area of single sheets which hence maximizes the number of exposed catalytic sites and increased density of vacancies, observed with transmission electron microscopy, during synthesis and processing.**

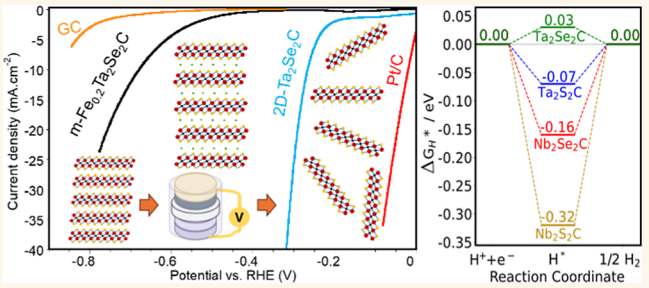

KEYWORDS: *two-dimensional materials, transition metal carbo-chalcogenides, delamination, hydrogen evolution, electrocatalyst*

Transition metal dichalcogenides (TMDs) are layered structures consisting of a core transition metal layer bonded to two surface layers of chalcogen atoms with a general chemical formula of MX_2 (M: transition metal, X: chalcogen such as S, Se, or Te).[1] These materials have direct bandgaps and interesting electronic and optical properties, which make them suitable candidates for various applications such as electronics[2] and optoelectronics.[3] Monolayers of TMDs were shown to be catalytically active with different electrical properties ranging from insulating to semiconducting and metallic, leading to their applications in electrochemical energy storage,[4] electrocatalysis,[5,6] heterogeneous catalysis,[7] and photocatalysis.[8] Especially 1T and 1T′ phases showed high electrical conductivity and have been reported as outstanding electrocatalysts for the hydrogen evolution reactions (HERs). For example, Lukowski et al.[9] reported the synthesis of 1T-MoS_2 using lithium intercalation and chemical exfoliation of 2H−MoS_2 that showed a low overpotential of 187 mV for a current density of 10 mA·cm^{-2}. In another study, Voiry et al. reported exfoliation of 1T-MoS_2 nanosheets with a Tafel slope of 40 mV·dec^{-1}.[10] TMDs are known to be earth-abundant materials as potential replacements for noble metal-based catalysts in the electrocatalytic HER,[5,11,12] due to their unique atomic structure and optimized active site density and surface area. However, these 2D-TMDs suffer from poor stability when exposed to ambient conditions. These materials, particularly in their monolayer or few-layer forms, are prone to oxidation and degradation upon exposure to air and moisture, which can significantly alter their electronic properties and hinder their performance in different applications.[13] For example, oxidation can result in the formation of metal oxides, disrupting the pristine crystalline structure and impairing conductivity. Additionally, defect sites in the crystal lattice, such as vacancies or grain boundaries, can exacerbate the degradation process, making these materials more susceptible to environmental stressors. Various approaches, such as encapsulation with stable 2D materials (e.g., graphene or hexagonal boron nitride) or functionalization with protective coatings, are being explored to mitigate these stability issues. Improving the stability of 2D-TMDs remains a critical challenge for their use in long-term and practical applications like flexible electronics and optoelectronic devices.[13,14] An alternative approach is the synthesis of new 2D materials that have high electrical conductivity, high catalytic activity, and higher stability at the same time. For instance, if we can synthesize 2D layered materials with a

Received: July 22, 2024
Revised: December 26, 2024
Accepted: December 30, 2024
Published: January 16, 2025

Scheme 1. Schematic Illustration of the Synthesis Procedure of 2D-Ta_2Se_2C

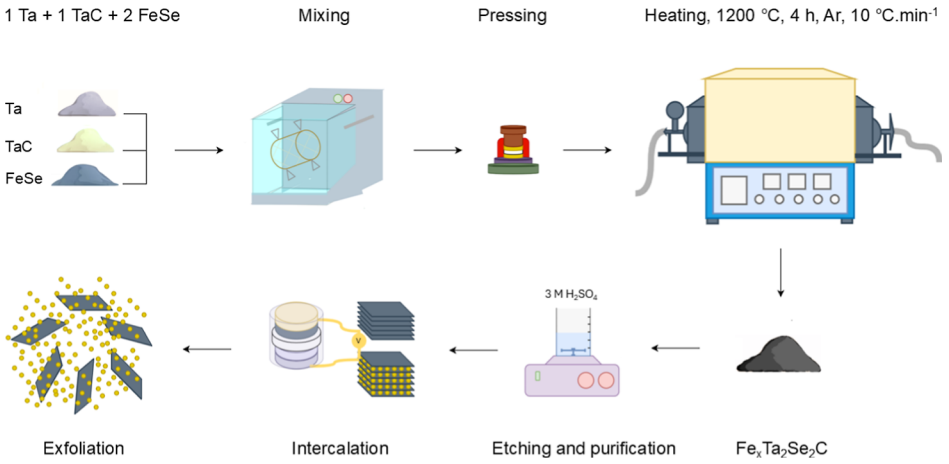

chalcogenide surface like TMDs and the carbide core of MXenes,[15] the resulting material could have extraordinary electrocatalytic performance owing to the combination of high catalytic activity, electrical conductivity, and high stability.

Recently, we reported on the large-scale synthesis of layered transition metal carbo-chalcogenides (TMCCs) and their exfoliation, including 2D-Ta_2S_2C and Nb_2S_2C, with superconductivity characteristics, high elastic constants, and promising performance as electrode materials in Li-ion batteries. TMCCs (M_2X_2C; M: transition metal, X: chalcogen, C: carbon) are a family that exhibits different properties and applications by tuning their composition.[16] This family has the potential to expand by using different transition metals, as well as different chalcogens. The first successful synthesis of the TMCC multilayer was reported for Ta_2S_2C in 1970 by Beckmann et al.[17] Later, more reports on the synthesis of TMCCs were published, such as $M_xNb_2S_2C$ (M: V, Cr, Mn, Fe, Co, Ni, Cu)[18] and Nb_2S_2C.[19] Recently, many *ab initio* calculation studies have focused on predicting the properties of various TMCCs.[20−25] These materials have layered structures with strong covalent intralayer bonding and relatively weak van der Waals out-of-plane bonding,[25] which makes their exfoliation process possible, as reported for the first time for 2D-Ta_2S_2C and Nb_2S_2C by Majed et al. in 2022.[16]

Although theoretical calculations have predicted the stability and properties of many 2D-TMCCs, most experimental studies have only focused on structures with sulfur as the chalcogen. There are still many TMCCs that have never been synthesized or reported, such as those including selenium, tellurium, and/or a solid solution of sulfur, selenium, and/or tellurium.

Herein, we report the synthesis of 2D Ta_2Se_2C. As shown in Scheme 1, multilayered Ta_2Se_2C was produced by the solid-state synthesis of $Fe_xTa_2Se_2C$, followed by chemical etching of iron. To exfoliate these materials, lithium (Li) was electrochemically intercalated between the layers (electrochemical cell schematic is shown in Scheme S1). The Li-intercalated Ta_2Se_2C was then submerged in water and sonicated to induce swelling and exfoliation of the layers. 2D-Ta_2Se_2C exhibited superior performance as an electrocatalyst for HER compared to their multilayer counterparts. Density functional theory (DFT) calculations were performed to predict the possible active sites of Ta_2Se_2C and three other TMCCs for comparison.

RESULTS AND DISCUSSION

Characterization of Materials. Figure 1a shows the X-ray diffraction (XRD) patterns of the as-synthesized, etched, lithiated, and delaminated samples. FeSe was used as a source for Se to enable synthesis at temperatures above the boiling point of Se, similar to our previous work on Ta_2S_2C,[16] where FeS was used as a source for S and similar to what Chen et al.[26] reported for Ti_2SC. This approach allowed us to use a tube furnace at ambient pressure, avoiding the need to seal the precursors in quartz tubes under vacuum and limiting the heating to temperatures below 1200 °C. Solid-state synthesis of $Fe_xTa_2Se_2C$ with the highest possible purity was crucial for the successful synthesis of the corresponding multilayer and delaminated Ta_2Se_2C. Details on the different synthesis parameters (precursors composition, time, and temperature) considered in the synthesis of $Fe_xTa_2Se_2C$ are provided in Supporting Information (Table S1 and Figure S1). We found that the optimum conditions for achieving the highest content of $Fe_xTa_2Se_2C$, relative to the secondary phases of Fe, TaC, and Fe_xTaSe_2, are a molar ratio of Ta/TaC/FeSe = 1.0:1.0:2.0 and a heating to 1200 °C for 4 h under continuous Ar flow. A characteristic XRD peak for $Fe_xTa_2Se_2C$ with the $P\bar{3}m1$ space group was found at a 2θ of ~9.96°, which is very close to what was reported for $Fe_xTa_2S_2C$.[16]

To remove the secondary phase of iron as well as intercalated iron from between the layers, we used a H_2SO_4 treatment. To confirm the removal of Fe, we used an EDS analysis (Table S3). The results showed a drop in the Fe: Ta atomic ratio from 1.00:1.00 to 0.09:1.00 after H_2SO_4 treatment, proving Fe was removed mostly from the sample. Hence, $Fe_{0.2}Ta_2Se_2C$ is used as the chemical formula for the multilayer sample after etching. Scanning electron microscopy (SEM) images of the particles before (Figure S4a,b) and after (Figure S4c,d) etching showed that both samples exhibit layered morphologies.

Predicting that both Ta_2Se_2C and Ta_2S_2C have similar crystal structures but slightly different lattice parameters, they are expected to exhibit similar XRD patterns with slight shifts in the diffraction peaks' positions. Thus, we used the structure of the Ta_2S_2C phase (PDF#00−024−1258) and replaced S with Se to predict the XRD pattern of Ta_2Se_2C. Using Bragg's law, the $d_{spacing}$ of the different crystallographic planes in Ta_2Se_2C was calculated, and from there, the lattice parameters were calculated. The *a* and *c* lattice parameters were calculated

https://doi.org/10.1021/acsnano.4c09903
ACS Nano 2025, 19, 3185−3196

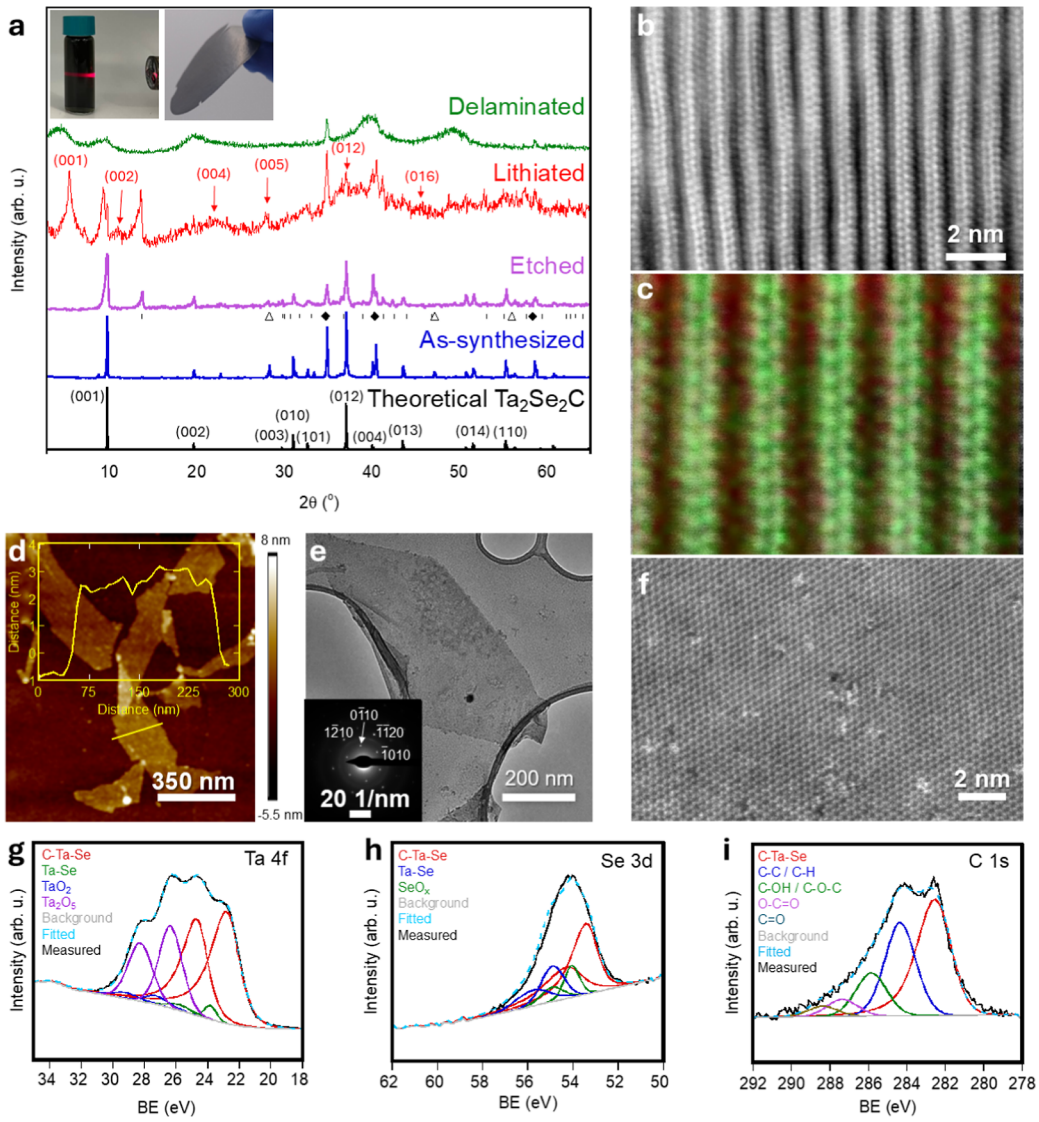

Figure 1. (a) XRD patterns of theoretical Ta_2Se_2C (black) and experimentally measured as-synthesized multilayer $Fe_xTa_2Se_2C$ before (blue) and after (purple) etching, then lithiated (red), and delaminated (green) Ta_2Se_2C. The peaks identified by ♦ indicate peaks for the TaC phase (PDF#00−035−0801), | indicate peaks for the $TaSe_2$ phase (PDF#21−1200), and Δ referred to Si used as reference. Insets: left, the Tyndall effect of the colloidal dispersion after delamination, and right, free-standing paper. (b) HAADF−STEM image of Ta_2Se_2C and (c) its corresponding EELS map overlay (green: Ta, red: Se), (d) AFM image of the 2D-Ta_2Se_2C few-layer sheets. Inset: height profile along the identified yellow line. (e) TEM image of 2D-Ta_2Se_2C single sheets. Inset: corresponding SAED pattern. (f) Atomically resolved STEM plan-view image of the 2D-Ta_2Se_2C. (g−i) XPS spectra of the Ta 4f, C 1s, and Se 3d regions, respectively, for 2D-Ta_2Se_2C.

to be 3.29 and 8.93 ± 0.05 Å, respectively. The XRD pattern based on these calculated lattice parameters was simulated using VESTA. The details for the peaks' positions and their corresponding crystallographic planes for the m-$Fe_{0.2}Ta_2Se_2C$ sample and the calculated data are provided in Table S2. To obtain a precise quantification for the phases present in the sample synthesized by the solid-state procedure as well as the lattice parameters, Rietveld refinement was employed (Supporting Information). According to the Rietveld refinement results, the *c*-lattice parameter stayed almost unchanged after the H_2SO_4 treatment ($\Delta c \approx 0.02$ Å decrease). We anticipated a decrease in the interlayer spacing after etching due to the removal of the Fe atoms from between the Ta_2Se_2C layers without the formation of new surface terminations as Ta atoms are already terminated by Se during the solid-state synthesis. This contrasts with typical 2D MXenes' synthesis, where the etching process (e.g., removal of Al from the Ti_2AlC MAX phase to form MXene) is accompanied by the introduction of new surface terminations, such as −OH, −O, or −F groups, which leads to an increase in interlayer spacing compared to the parent MAX phases. The behavior of Fe-intercalated Ta_2Se_2C is predicted to be more analogous to that of intercalated MXenes rather than MAX phases. For intercalated MXenes, deintercalation results in a decrease in interlayer spacing.[27,28] The small change in the *c*-lattice parameter after H_2SO_4 treatment suggests that the presence of a small amount of iron might be sufficient to maintain the interlayer spacing for the Ta_2Se_2C structure; similar behavior was reported for intercalated 2D materials where a small amount of intercalants can act as pillars maintaining the interlayer spacing.[27−30]

XRD after etching revealed a more pronounced peak at 2θ of 13.86° that can be assigned to $TaSe_2$ (PDF#21−1200). This

https://doi.org/10.1021/acsnano.4c09903
ACS Nano 2025, 19, 3185−3196

phase already existed in the $Fe_xTa_2Se_2C$ sample, but after etching and purification, its peaks grew in intensity.

A high-resolution cross-sectional high-angle annular dark field (HAADF)−scanning transmission electron microscopy (STEM) image of a m-$Fe_{0.2}Ta_2Se_2C$ particle together with a corresponding electron energy loss spectroscopy (EELS) elemental map overlay are shown in Figure 1b,c. These images illustrate layered sheets that consist of two atomic layers of tantalum sandwiched between two atomic layers of selenium. The EELS quantification revealed a Ta: Se molar ratio of 2.0:1.8 (Table S4 and Figure S5a), where the deviation from the 2.0:2.0 ratio can be explained by the formation of Se vacancies during acid etching. The interlayer spacing determined from the HAADF−STEM image was found to be 0.98 ± 0.02 nm. The slight difference between TEM (0.98 nm) and XRD (0.89 nm) interlayer spacings likely arises from the localized nature of TEM compared to the bulk averaging of XRD, as well as peak broadening or asymmetry in the XRD data due to sample inhomogeneity or restacking.

The XRD pattern of Li/*m*-$Fe_{0.2}Ta_2Se_2C$ after electrochemical lithiation (voltage profile is shown in Figure S3) indicated a significant shift in the (00*l*) peaks toward lower angles (Figure 1a). The (001) peak at a 2θ of 9.96° shifted to about 5.52°, indicating an increase in $d_{spacing}$ of 0.71 nm, which is due to the intercalation of Li between the layers. Here, we also noticed the peaks related to m-$Fe_{0.2}Ta_2Se_2C$ (at $2\theta \sim 9.8°$) and $TaSe_2$ (at $2\theta \sim 13.8°$) structures, suggesting the presence of some unintercalated m-$Fe_{0.2}Ta_2Se_2C$ and $TaSe_2$ in the sample. After Li-intercalation, deionized (DI) water was added to the sample while starting sonication. The addition of water results in the formation of LiOH (which is water-soluble) and H_2 gas. The mechanical force from ultrasonic-induced cavitation of the H_2 bubbles leads to the exfoliation of the layers.[28] After exfoliation, centrifuging the sample led to the separation of the few-layer sheets in the supernatant from multilayer particles and secondary phases in the precipitate. The inset in Figure 1a shows the supernatant exhibiting the Tyndall effect, suggesting the formation of a colloidal dispersion and a free-standing paper obtained after vacuum-assisted filtration of the supernatant. A cross-sectional SEM image of the free-standing paper, shown in Figure S4g, reveals restacked layers due to vacuum-assisted filtration. XRD for the free-standing paper of 2D-Ta_2Se_2C (Figure 1a) shows a broadening and significant shifting of the early peak at 9.96° for m-$Fe_{0.2}Ta_2Se_2C$ toward a lower angle of about 4.68°, which is due to the exfoliation of the multilayer structure to monolayers. Observation of broad and low-intensity. XRD peaks at lower angles in the 2D-Ta_2Se_2C paper indicate a less ordered restacking of the delaminated layers during the vacuum-assisted filtration process used to form the free-standing paper. All of the peaks, as marked in the XRD pattern, correspond to different (00*l*) planes of the Ta_2Se_2C phase. The peak at 35.07° corresponds to (111) planes of the TaC phase (PDF#00−035−0801). Freeze-drying the supernatant results in the formation of an aerogel. The SEM images for the aerogel sample in Figure S4e,f indicate a flaky morphology in the microscale, suggesting single- and/or few-layer sheets indicating the success of the delamination step. Figure 1d illustrates a few-layer sheet of Ta_2Se_2C captured by AFM. The height profile for an identified scan line is shown in the inset of Figure 1d. From the height profile, the sheet thickness was determined to be <4 nm, which indicates the measured sheet has few layers of thickness.

To gain better insight into the morphology and structure of 2D-Ta_2Se_2C, we used TEM and selected-area electron diffraction (SAED). Figure 1e shows a TEM image of a single sheet and the corresponding SAED pattern indicating the hexagonal symmetry which means the material has preserved its structure through the lithiation and exfoliation processes.[16,31,32] The SAED pattern of 2D-Ta_2Se_2C reveals a well-ordered hexagonal symmetry inherited from m-$Fe_{0.2}Ta_2Se_2C$, characteristic of high crystallinity. The HAADF−STEM plan-view image of a single layer, shown in Figure 1f, reveals a honeycomb arrangement of atoms. This is directly related to the arrangement of the Ta atoms, which dominate the image contrast through the Z^2 mechanism, in agreement with the SAED pattern. Figure S5b shows the individual and mixed elemental maps from STEM−EELS, with Ta in green and Se in red, revealing distinct alternating layers of Ta and Se, highlighting the layered structure characteristic of 2D-Ta_2Se_2C. Figure S5c,d presents a magnified view of the HAADF−STEM plan-view image of a single sheet of 2D-Ta_2Se_2C, along with its corresponding fast Fourier transform pattern. The atomic arrangement reveals a Ta−Ta spacing of 2.5 Å. Atomic defects such as vacancies and pinholes can be observed as dark spots, which can be useful as anchoring sites for single-atom catalysts as well as for tuning the material's properties, similar to what has been reported for other 2D materials.[32−36] More TEM images of 2D-Ta_2Se_2C are provided in Figure S6a−d.

We used XPS measurements to gain a better understanding of the chemical nature of the elements on the surface of the sample and the chemical composition of the 2D sample. The survey spectrum (Figure S7) from −10 to 1350 eV indicated the presence of Ta, Se, C, Fe, Li, and Cu in the sample. High-resolution XPS spectra for the Ta-4f region (Figure 1g) can be deconvoluted using 8 peaks. The doublets at 22.6 and 24.69 eV correspond to $4f_{7/2}$ and $4f_{5/2}$, respectively. These peaks were assigned to Ta_2Se_2C since they are located between the peaks for TaC[36] and $TaSe_2$.[37,38] The peaks at 23.2 and 25.74 eV correspond to $TaSe_2$.[37,38] The peaks at 29.14 and 26.36 eV originated from TaO_2[39] and Ta_2O_5[40] oxides with doublets at 28.27 and 29.14 eV, respectively. These oxides could have formed after the solid-state synthesis as native oxides like what has been reported for layered carbides,[41,42] during etching, delamination, and/or sample preparation for XPS. The high-resolution XPS spectra for the Se-3d region (Figure 1h) can be fitted using 6 main peaks. The peaks at 53.4 and 54.3 eV correspond to $3d_{5/2}$ and $3d_{3/2}$, respectively. These peaks were assigned to Ta_2Se_2C.[16] The other doublets at 54.05 and 54.91 eV are related to $TaSe_2$. The peaks at 55.76 and 55.89 eV correspond to SeO_x.[43,44] $TaSe_2$ was formed during the solid-state synthesis process and the SeO_x peak is related to surface oxidation that can occur during etching and or delamination, handling, and or sample preparation for XPS measurements, which leads to Se vacancy formation.[43] Fitting the C 1s spectrum in Figure 1i resulted in five peaks. The peak at 282.6 eV was assigned to Ta_2Se_2C. The second peak at higher binding energy, located at 284.4 eV, is related to the C 1s peak for C−C and or C−H chemical bonds.[45] The peaks at 285.9, 287.4, and 288.4 eV were related to C−OH or C−O−C, C═O, and O−C═O, respectively.[45,46]

The high-resolution XPS spectra of the Fe 2p region (Figure S8) were very weak, indicating the small amount of Fe in the sample with a Fe/Ta molar ratio of 0.196:1.00 obtained from XPS quantification (Table S5), and in agreement with EDS

https://doi.org/10.1021/acsnano.4c09903
ACS Nano 2025, 19, 3185−3196

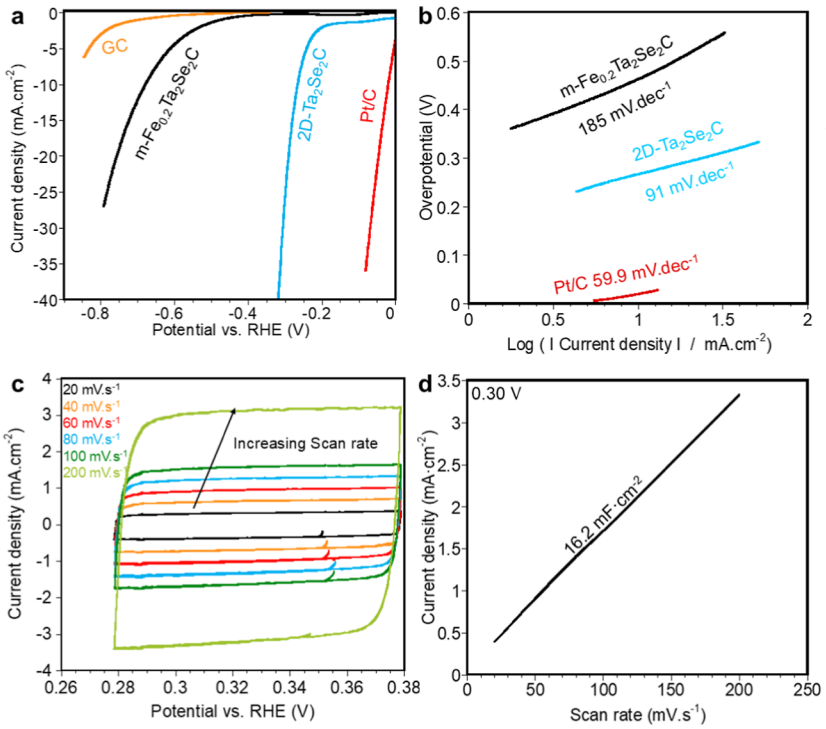

Figure 2. Electrochemical performance of Ta_2Se_2C as an electrocatalyst for HER. (a) LSV curves for glassy carboy (GC), Pt/C, m-$Fe_{0.2}Ta_2Se_2C$, and 2D-Ta_2Se_2C with H_2 bubbling after 20 CVs at OCP ± 50 mV in a 3-electrode cell with a 0.5 M H_2SO_4 electrolyte with Hg/Hg_2SO_4 in saturated K_2SO_4 as the reference electrode and Pt wire as the counter electrode. (b) Tafel polarization curves derived from LSV curves for m-$Fe_{0.2}Ta_2Se_2C$ and 2D-Ta_2Se_2C. (c) CVs at different scan rates of 20, 40, 60, 80, 100, and 200 mV·s^{-1} at the potential window of 0.28−0.38 V (OCP ± 50). (d) Current density versus scan rate plot corresponding to 0.30 V extracted from CVs at different scan rates.

(Table S3) and inductively coupled plasma mass spectrometry (ICPMS) (Table S6) results. The observed increase in relative Fe content in the delaminated sample is likely due to the removal of TaC during the delamination process, which does not contain Fe. This results in a relative enrichment of Fe in the remaining sample despite the absolute Fe content remaining unchanged.

The Fe 2p region can be resolved into two main peaks corresponding to Fe^0 and Fe^{3+} (Fe_2O_3) at 706.9 and 709.5 eV, respectively, along with their associated doublets at 719.7 and 722.7 eV, respectively. Since Li 1s overlaps with Se 3d, it was not possible to study Li using XPS. Thus, we used ICPMS (Table S6) to quantify the residual Li content in the 2D-Ta_2Se_2C sample and found the molar ratio of Li/Ta to be 0.38:1.00.

The UV−vis spectra for m-$Fe_{0.2}Ta_2Se_2C$ and 2D-Ta_2Se_2C in DI water are shown in Figure S10, clearly illustrating differences in absorption behavior. While both materials exhibit strong UV absorbance, 2D-Ta_2Se_2C retains significantly higher absorbance in the visible and near-infrared regions than m-$Fe_{0.2}Ta_2Se_2C$ and Ta_2O_5.[46] According to the literature, Ta_2O_5[46,47] displays minimal absorbance beyond the UV range, typical of a bulk wide-bandgap insulator. The enhanced visible and near-infrared absorbance in 2D-Ta_2Se_2C suggests quantum confinement effects or surface plasmon resonances, which are absent in the bulk-like m-$Fe_{0.2}Ta_2Se_2C$ and Ta_2O_5.[46,47] The higher absorbance for 2D-Ta_2Se_2C across the visible spectrum, compared to both m-$Fe_{0.2}Ta_2Se_2C$ and Ta_2O_5,[46,47] may be attributed to the unique electronic and structural properties introduced by the 2D exfoliation process, leading to increased light−matter interactions and potentially more active sites for electronic transitions.[48] However, the semifeatureless UV−vis might be explained by the presence of other bulk phases coexisting with delaminated materials.[49] These bulk phases are most likely TaC, which was detected in the XRD patterns after delamination and centrifugation. Additionally, a small amount of undelaminated m-$Fe_{0.2}Ta_2Se_2C$ particles which cannot be detected in the XRD patterns might also coexist with the delaminated materials. Thus, further systematic studies are required to purify the samples after delamination and to eliminate any bulk phases. Such studies might involve varying sonication time and frequency, centrifugation speed, and solvent type.[50]

The electrical conductivity values obtained using the four-probe method are listed in Table S7. For m-$Fe_{0.2}Ta_2Se_2C$, the conductivity was found to be 2.75 S·cm^{-1}, but it dropped to 0.46 S·cm^{-1} after delamination (2D-Ta_2Se_2C). However, 2D-Ta_2Se_2C shows a slightly higher electrical conductivity than 2D-$TaSe_2$ (0.41 S·cm^{-1}). Potentiostatic electrochemical impedance spectroscopy (PEIS) measurements (Figure S9e) reveal the same trend with lower resistance for m-$Fe_{0.2}Ta_2Se_2C$ (0.38 Ω·cm^2) compared to that for 2D-Ta_2Se_2C (0.58 Ω·cm^2) and 2D-$TaSe_2$ (0.71 Ω·cm^2). Here, we also see a slightly lower resistance for 2D-Ta_2Se_2C compared to that for 2D-$TaSe_2$. This behavior is explained by the oxidation of samples during the etching and delamination, as well as the loss of van der Waals interactions between layers, reducing electron mobility, while selenium vacancies introduce midgap defect states that trap charge carriers and further hinder conductivity. These vacancies are particularly detrimental in both Ta_2Se_2C and $TaSe_2$, correlating with the sharp decline in conductivity, as they disrupt the metallic interlayer coupling and charge transport pathways, a phenomenon observed across many TMD systems.[51] However, multilayer and delaminated $TaSe_2$

https://doi.org/10.1021/acsnano.4c09903
ACS Nano 2025, 19, 3185−3196

and Ta_2Se_2C samples show low electrical conductivities across all samples, largely probably due to selenium vacancies and oxidation of the samples introduced during the etching process used to remove intercalated Fe atoms.

Electrocatalytic Performance for HER. Here, we focused on the electrochemical performance of Ta_2Se_2C as an electrocatalyst for HER. Figure 2a illustrates the linear sweep voltammetry (LSV) diagrams for m-$Fe_{0.2}Ta_2Se_2C$ and 2D-Ta_2Se_2C when used as an electrocatalyst for HER while bubbling H_2. LSV values for glassy carbon (GC) and Pt/C electrodes were also plotted for comparison. The LSV diagrams were collected after 20 cyclic voltammograms (CVs) in the range of open-circuit potential (OCP) ± 50 mV to eliminate the effect of any possible reactions in the system during LSV measurements. The LSV was carried out in a 3-electrode cell using H_2 gas bubbling. The overpotential (η_{10}) of Ta_2Se_2C decreased from 678 to 264 mV due to delamination from m-$Fe_{0.2}Ta_2Se_2C$ to 2D-Ta_2Se_2C, respectively. The two distinct slopes in the LSV for the delaminated sample, with significant current observed in the 0 to −0.3 V range, indicate an increased surface area and a higher density of active sites compared to the multilayer sample. The early onset of current can be attributed to better accessibility to catalytic sites or surface defects introduced by the delamination process, as suggested by previous studies on the effect of increased surface area and delamination on catalytic performance.[52] Since the Pt counter electrode might affect the accuracy of overpotential measurements, especially in acidic electrolytes,[53,54] we repeated LSV measurements using a graphite rod counter electrode (Figure S9a). A slightly lower overpotential of 252 mV was observed compared to the LSV measurement using the Pt wire counter electrode (264 mV).

The promising performance of 2D-Ta_2Se_2C indicates that delaminating Ta_2Se_2C and exposing more catalytic active sites remarkably improve its performance for HER and is comparable to previously reported electrocatalysts for HER.[9,55−58] For example, Thangasamy et al. exfoliated MoS_2 powder using sonication at different dispersion media achieving an η_{10} of 570 to 720 mV.[55] In another study, Thangasamy et al. used a solvothermal approach to produce a rose-like shape MoS_2 nanostructure, resulting in an η_{10} of 330 mV.[55] Chen et al. synthesized TaS_2 by electrochemically exfoliating bulk TaS_2 using an alternating voltage in an acidic electrolyte, with an η_{10} of 370 mV on GC.[56]

To further understand the HER kinetics and inherent activities of m-$Fe_{0.2}Ta_2Se_2C$ and 2D-Ta_2Se_2C samples for the HER, Tafel polarization curves were plotted using data from LSV curves (Figure 2b). The Tafel slope for 2D-Ta_2Se_2C in the presence of H_2 gas in the system was calculated to be 91 $mV{\cdot}dec^{-1}$, indicating the HER kinetics is controlled by the Volmer step[57] and much lower than m-$Fe_{0.2}Ta_2Se_2C$ (185 $mV{\cdot}dec^{-1}$). This indicates the higher intrinsic activity of 2D-Ta_2Se_2C due to the synergistic effect of the large, exposed surface area, the presence of iron as single atoms, and vacancies in the structure, which provide a more open structure. As reported in the literature for TMDs, vacancies enhance the catalytic activity in HERs by creating active sites and altering the electronic structure. Sulfur (S) and Selenium (Se) vacancies in 2D-TMDs lower hydrogen adsorption energy, making the surface more reactive and improving the efficiency of hydrogen adsorption and desorption.[58] These vacancies also increase the number of available edge sites, which are crucial for efficient HER catalysis. Similarly, in TMCCs, tuning the vacancy concentration can potentially optimize the catalytic performance of 2D-TMCCs, making them promising candidates to replace noble metal catalysts in the HER. Understanding the role of Se vacancies in 2D-Ta_2Se_2C is essential for enhancing its catalytic efficiency in hydrogen evolution. Further investigation into how these vacancies affect the material's electronic properties and catalytic activity will provide deeper insights into its performance and guide the development of more efficient catalysts for energy conversion applications.[58,59]

Then, CVs at different scan rates of 20, 40, 60, 80, 100, and 200 $mV{\cdot}s^{-1}$ were measured for 2D-Ta_2Se_2C (Figure 2c) with bubbling H_2. H_2 purging was performed to saturate the electrolyte, ensuring a consistent electrocatalytic performance. To confirm that this does not affect the accessibility to active sites, we measured the CVs with and without bubbling H_2, and the results were nearly identical (Figure S9b). The CVs show almost the same capacitance, indicating that the low flow rate of H_2 bubbling used in this experiment does not hinder the accessibility of the active sites. By extracting the values of the difference between anodic and cathodic current densities at 0.30 V corresponding to different scan rates, we obtained the plot in Figure 2d. Assuming no Faradaic reaction contribution, the slope of this line is equal to the double-layer capacitance (C_{dl}).[60] A C_{dl} of about 16.2 $mF{\cdot}cm^{-2}$ was measured, corresponding to a specific electrochemically active surface area (ECSA) of 17.61 $m_{ECSA}{}^2{\cdot}g_{catalyst}{}^{-1}$ (details of the calculations and assumptions are provided in the Supporting Information). Compared to the theoretical specific surface area of 212.82 $m^2{\cdot}g^{-1}$, the lower ECSA estimated here suggests incomplete utilization of Ta_2Se_2C or that the basal plane might not be the active site for HER. The ECSA and C_{dl} values are higher than what was reported for ultrathin $Ti_3C_2T_x$ MXene (ECSA = 12.07 $m_{ECSA}{}^2{\cdot}g_{catalyst}{}^{-1}$), MoS_2 (2 $m_{ECSA}{}^2{\cdot}g_{catalyst}{}^{-1}$),[55] and $TaSe_2$ nanobelts (13.12 $m_{ECSA}{}^2{\cdot}g_{catalyst}{}^{-1}$),[61] indicating the high effective surface area of the 2D-Ta_2Se_2C electrocatalyst. Table S8 compares the electrocatalytic performance of 2D-Ta_2Se_2C with various 2D-TMDs reported in the literature, demonstrating that 2D-Ta_2Se_2C exhibits a performance on par with some of the most active 2D-TMDs. Also using CVs at different scan rates, the capacitance versus potential graph was extracted (Figure S9c), demonstrating uniform capacitance behavior across the scan rates.

The chronoamperometric stability graph for D-Ta_2Se_2C in Figure S9d reveals promising electrochemical stability under continuous operation at room temperature under H_2 bubbling at a constant applied potential of −0.3 V. The initial sharp decrease in current density observed in the first few hundred seconds likely represents the formation of a stable electrochemical double layer and the initial activation of surface sites. Following this, the current stabilizes, with a gradual increase, suggesting that the material undergoes further surface restructuring or stabilization of active sites, improving its conductivity and catalytic activity over time. Importantly, the absence of significant fluctuations or current decay throughout the 1500 s test indicates that 2D-Ta_2Se_2C exhibits durable electrochemical performance without apparent degradation. This stable behavior suggests that 2D-Ta_2Se_2C can maintain its activity over extended electrochemical cycles, making it a strong candidate for applications requiring sustained electrochemical activity, such as in energy conversion or storage technologies.

https://doi.org/10.1021/acsnano.4c09903
ACS Nano 2025, 19, 3185−3196

To compare the chemical stabilities of 2D-Ta_2Se_2C and 2D-$TaSe_2$, the colloidal dispersion obtained after delamination was stored at room temperature for several days, and photographs were taken at different time intervals (Figure S11). The results showed that the 2D-$TaSe_2$ solution began to change color within the first few hours, indicating lower stability compared to that of 2D-Ta_2Se_2C, which exhibited almost no color change even after several days.

The turnover frequency (TOF) versus potential graph obtained from the LSV results for 2D-Ta_2Se_2C in Figure S9f shows that the TOF increases as the applied overpotential increases from −0.2 V vs reversible hydrogen electrode (RHE) to more negative (−0.38 V vs RHE). This suggests that the catalytic activity improves significantly at more negative potentials, indicating an enhanced reaction kinetics in this region. The red plot is when we consider the Se sites at the edge to be active (0.4% of the total amount of Se), and the blue plot is when we consider the Se sites at the basal plane to be active (details of the calculations and assumptions are provided in the Supporting Information).

It is worth noting that, as discussed earlier, bulk phases such as TaC particles, which are not known to be effective catalysts for HER,[62] coexisted with delaminated Ta_2Se_2C. Therefore, it is reasonable to predict that better performance can be achieved by further purifying the sample and synthesizing higher-purity materials. Another factor that might contribute to the electrocatalytic behavior of the studied materials is the presence of small amounts of lithium and iron in the sample. Iron is known to be an effective catalyst for HER, particularly when used as a single-atom catalyst.[63] For instance, an overpotential as low as 9 mV and a favorable Tafel slope of 37.8 mV·dec^{-1} were reported for iron/graphdiyne.[64] However, the iron residues from the solid-state synthesis step of bulk Ta_2Se_2C, which persisted in the materials after delamination, are not expected to lead to single-atom dispersion of iron on the surface of Ta_2Se_2C sheets. Instead, they likely form particles of iron and iron oxide, as observed through XPS analysis. Further studies are needed to understand the nature of iron and lithium in TMCCs and their effect on the electrochemical behavior of TMCCs.

DFT Calculations. To gain atomistic insight into the reactivity trends and the likely active sites, H adsorption on various TMCCs (Ta_2Se_2C, Ta_2S_2C, Nb_2Se_2C, and Nb_2S_2C) was calculated by DFT. The TMCCs were modeled including an edge so that both edge and plane sites could be studied. One H atom was placed at various positions, and 5 relatively low-energy converged structures were found, as shown in Figure 3a. H(1) is on top of a surface S/Se, similar to adsorption on the basal plane of a 2D surface; H(3) is bridging an S/Se and a metal atom at the edge; H(4) is on top of a metal atom at the edge; H(2) and H(5) are binding to two different edge S/Se atoms. The calculated ΔG_{H^*} values at these 5 positions for the four TMCCs are listed in Table S9. Among the 5 positions, H(5) always had the strongest adsorption, and its ΔG_{H^*} was the closest to 0. This indicates that H(5), an S or Se edge site, is likely to be most active for HER. The ΔG_{H^*} of H(5) on 4 TMCC edges are shown in Figure 3b, with an order of Ta_2Se_2C > Ta_2S_2C > Nb_2Se_2C > Nb_2S_2C. The results indicate that the TMCC with Nb has stronger adsorption than Ta, and S has stronger adsorption than Se. Ta_2Se_2C is the nearest to the zero level, which suggests it would have the highest catalytic performance for HER among the 4 materials. The Ta_2Se_2C sites have an H adsorption energy quite close to 0, which might be expected to lead to an overpotential close to 0. However, the H adsorption energy alone is not quantitatively accurate in predicting electrocatalytic performance, as the details of the mechanism and transition states and the effect of the complex electrocatalytic environment all play a role in determining the performance.[65]

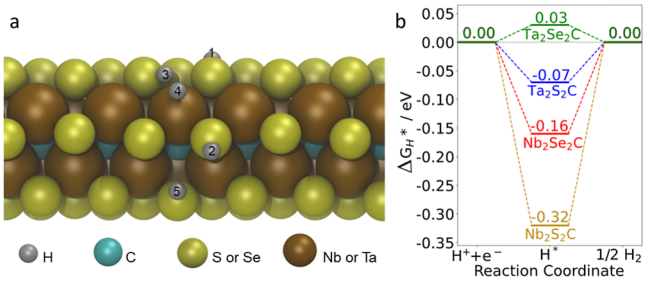

Figure 3. (a) Side view of H adsorption on different positions of a TMCC edge. (b) ΔG_{H^*} of H(5) on different TMCC edges.

To gain insight into how the C core may generally lead to conductivity in TMCCs, we calculated the projected density of states (PDOS) for Ta_2Se_2C and 1H−$TaSe_2$ (Figure S12). 1H−$TaSe_2$ is itself metallic, and our calculations correctly capture this (see Figure S12b) as do previous calculations.[66] Our calculations also correctly predict Ta_2Se_2C to be metallic (see Figure S12a). In Ta_2Se_2C, we found that the C core did not directly contribute to a large number of states in the region around the Fermi energy but instead modified the PDOS on the other two elements. Specifically, $TaSe_2$ shows more isolated peaks with gaps between them, while for Ta_2Se_2C, there is more overlap between peaks and fewer gaps. This smoother behavior with few gaps was also seen in previous PDOS calculations of TMCCs.[67] This reduction in the number of gaps would be expected to generally promote metallic behavior, consistent with the more metallic nature of TMCCs as compared to TMDs.

CONCLUSIONS

In summary, to obtain efficient electrocatalysts containing core carbon layers of MXenes which provide high electrical conductivity as well as stability and the surface layer of TMDs which provides high electrochemical activity, we produced multilayer Ta_2Se_2C for the first time through a simple scalable and rapid solid-state thermal process under atmospheric pressure. Ta, TaC, and FeSe were mixed, pressed, and heated for 4 h at 1200 °C. Most of the iron in the secondary phase and the iron between the layers were removed by etching in 3 M H_2SO_4. Electrochemical Li-intercalation followed by sonication in DI water exfoliation led to the synthesis of Ta_2Se_2C mono-/few-layer sheets. Comparing measured and theoretically calculated XRD patterns confirmed the formation of the hexagonal Ta_2Se_2C structure ($P\bar{3}m1$ space group). Microscopy techniques illustrated the layered hexagonal structure of the multilayer sample and few-layer sheets for the delaminated sample with about 4 nm thickness. STEM−EELS quantified a Ta/Se ratio of almost 2.0:1.8, suggesting Se vacancies in the structure most likely formed during the purification and liquid exfoliation procedures.

We investigated the electrocatalytic performance of the drop-casted sample on a GC electrode which illustrated an improved HER electrocatalytic performance of 2D-Ta_2Se_2C (η_{10} = 264 mV), compared to the multilayered Ta_2Se_2C (η_{10} =

https://doi.org/10.1021/acsnano.4c09903
ACS Nano 2025, 19, 3185−3196

678 mV), due to a synergistic effect of inherent catalytic performance of the material possibly as a result of high electrical conductivity and catalytic activity, and an ECSA of about 17.61 m_{ECSA}^{2} $g_{catalyst}^{-1}$. Using DFT calculations to analyze reactivity trends and active sites for H adsorption on various TMCCs, we identified five potential active sites, with the strongest adsorption occurring at the binding edge S/Se atoms, exhibiting an adsorption free energy of 0.03 eV. This suggests that these sites are the most active for HER. Comparison among different TMCCs revealed Ta_2Se_2C as the top performer for HER catalysis, with the order of catalytic activity as Ta_2Se_2C > Ta_2S_2C > Nb_2Se_2C > Nb_2S_2C.

Our study proposes a scalable synthesis method for multilayer and 2D-TMCCs or TMCC nanoparticles, facilitating the design of efficient electrocatalysts for the HER and likely other energy storage applications.

EXPERIMENTAL SECTION

Synthesis of Multilayer $Fe_xTa_2Se_2C$. A simple solid-state method was used to synthesize $Fe_xTa_2Se_2C$. In a typical procedure, Ta (Alfa Aesar, <44 μm, 99.9% purity), TaC (Alfa Aesar, <44 μm, 99.9% purity), and FeSe (Thermo Scientific, <420 μm, 99.9% purity) powders were weighed in an argon (Ar)-filled glovebox under an ultrahigh-purity (UHP) Ar atmosphere. Powders in the molar ratio of Ta/TaC/FeSe = 1.0:1.0:2.0 (each batch was 10 g) were placed in a 30 mL high-density polyethylene (HDPE) jar containing 20 yttrium-stabilized zirconia balls of 5 mm diameter each. The HDPE jar was closed and sealed using parafilm and removed from the glovebox for mixing. A Turbula T2F mixer at ≈56 rpm for 3 h was used to mix the powders. Then, the jar was transferred to the glovebox again, and the powders were pressed into a 1″ diameter pellet under 350 bar, put in an alumina crucible, and transferred in a sealed container to a tube furnace that was in a well-ventilated chemical fume hood. The sample was heated to 1200 °C at a heating rate of 10 °C·min^{-1} and held at 1200 °C for 4 h, and then the furnace was allowed to cool to room temperature. The heating and cooling treatments were carried out under a continuous Ar flow of about 3 L·min^{-1}. Other synthesis conditions for $Fe_xTa_2Se_2C$, including different precursor compositions, synthesis temperatures, and times, were explored and are listed in the Supporting Information (Table S1). The method used to synthesize Fe_xTaSe_2 is explained in Supporting Information and the corresponding XRD plot is provided in Figure S2.

To remove excessive iron, the sample was ground to −325 mesh (<44 μm), and 1 g of $Fe_xTa_2Se_2C$ powder was gradually added to 20 mL of 3 M H_2SO_4 and stirred for 24 h at room temperature. The mixture was sonicated every few hours for 1 min to facilitate acid penetration into the powder particles with a total sonication duration of 5 min. Then, the acid was replenished, and the procedure was repeated for another 24 h. Then, the solution was centrifuged at 3500 rpm for 3 min, the acid was decanted, and settled powders were washed with DI water to pH ≈ 7 and vacuum filtered on a Whatman filter paper grade 2 overnight.

Synthesis of 2D-Ta_2Se_2C. To exfoliate the layers of Ta_2Se_2C and obtain single- or few-layer sheets, we used the electrochemical Li-intercalation technique (voltage profile in Figure S3) followed by exfoliation via sonication in DI water. About 120 mg of the multilayer powder was pressed to a free-standing 1″ diameter wafer under 500 bar. The wafer was transferred to an Ar-filled glovebox (O_2 < 0.1 ppm, H_2O < 0.1 ppm). The schematic configuration of the electrochemical cell (EL CELL) is shown in Scheme S1. A stainless-steel disk of 14 mm diameter was used as the bottom-part current collector. Both sides of a Li wafer were brushed to get a shiny surface and pressed on the stainless-steel disk to attach to it and get a mirror-like surface. A glass microfiber filter (Whatman CAT no. 1823−047 GF/D, 2.7 μm) was placed on the Li wafer, and 100 μL of 1 M $LiPF_6$ in ethylene carbonate and ethyl methyl carbonate (EMC) (EC/EMC equaled 3:7 by volume) was dropped all over the separator as an electrolyte. Then, the free-standing wafer and a copper foil of 1″ diameter were added as the working electrode and current collector, respectively. The cell was sealed tightly, removed from the glovebox and connected to a potentiostat−galvanostat (VMP3, BioLogic). Galvanostatic cycling with potential limitation (GCLP) was conducted with a low discharge rate of 5 mA·g^{-1} started from the OCP to a cutoff potential of 0.1 V vs Li/Li^+. During discharge, Li intercalates between the layers of Ta_2Se_2C. Figure S3 shows the voltage profile for a 120 mg wafer. After reaching the cutoff potential, the EL CELL was disconnected and transferred to the glovebox, and the working electrode was removed from the EL CELL, soaked in diethyl carbonate (DEC) to rinse off any remaining salts, removed from DEC, cleaned gently with Kimwipe, and then put in a 50 mL centrifuge tube. The tube cap was tightened before removal of the tube from the glovebox and transferred to an ultrasonic bath. Sonication at 37 MHz was started while adding 50 mL of DI water to the tube. A 5 min sonication followed by one h centrifugation at 5000 rpm was conducted as the first cycle. The supernatant was separated and discarded, 50 mL of DI water was added to the sediment and redispersed, and the second cycle was conducted with 5 min sonication and a 30 min centrifugation at 3500 rpm. The supernatant was collected in a bottle. 50 mL of DI water was added to the sediment, and the previous cycle of sonication and centrifugation was repeated until a clear liquid was obtained after centrifugation. Finally, the collected liquid was filtered or freeze-dried. The material on the filter formed a free-standing paper, and the material from the freeze drier formed an aerogel. The schematic procedure used here for synthesizing 2D-Ta_2Se_2C is provided in Scheme 1.

Characterization of Multilayer and Delaminated Ta_2Se_2C. A Cu K_α X-ray diffractometer Rigaku D/Max-2200 was used to collect XRD patterns at a 2θ step size of 0.02° and a sweep rate of 1°·min^{-1} at operation conditions of 40 kV and 40 mA. SEM images were captured using a Hitachi S-4800 with an acceleration voltage of 3 kV. For elemental analysis, we used an SEM Hitachi S-3400 equipped with an energy-dispersive X-ray spectroscopy detector (EDS, Oxford, UK) at an accelerating voltage of 30 kV connected to INCA software. Elemental concentrations were determined using the Thermo Element2 high-resolution ICPMS at Tulane University's TINI department. Linear calibration curves were established for each element with a laboratory blank subtracted. The sample solution was prepared by dissolving 2D-Ta_2Se_2C in an aqua regia solution with hydrofluoric acid addition. Results were reported as parts per billion after appropriate dilution using 2% nitric acid. A solution of 0.6 g·L^{-1} was prepared, and UV−vis absorption spectra were recorded using a UV-1700 PharmaSpec UV−vis Spectrometer (Shimadzu Corporation), equipped with UVProbe software (Version 2.35) for data acquisition and analysis.

TEM images were captured by an FEI TECNAI G2-F30 transmission electron microscope at an accelerating voltage of 200 kV. To get a better understanding of the elemental composition and the atomic-scale configuration of the structure, EELS together with STEM imaging using a HAADF detector was carried out using the Linköping double C_s-corrected FEI Titan^3 60−300 microscope operated at 300 kV and the embedded GIF Quantum ERS. The probe maintained a convergence angle of 21.5 mrad throughout the imaging and EELS acquisition. EELS spectrum images (SIs) were acquired for 5 min using 0.1 nA beam current, 0.25 eV/channel energy dispersion, 0.2 s pixel dwell time, and a 55 mrad collection semiangle. To prepare the sample, a multilayer powder was mixed with distilled water to make a liquid suspension. Then the liquid suspension was sonicated for 2 min to break the large Ta_2Se_2C multilayers into small particles to avoid charging issues. A few drops from the liquid suspension were then dropped onto the copper lacey carbon grid (300 mesh) and allowed to dry for a few minutes. Then, the grid was loaded into a standard double-tilt holder and introduced into the microscope.

For surface chemistry investigation, we used X-ray photoelectron spectroscopy (XPS, Thermo Fisher, USA) with an Al K_α X-ray source at a 200 eV pass energy, a step of 1 eV, and a spot size of 400 μm. The XPS sample was prepared by drop-casting a diluted slurry of the aerogel sample in a nonaqueous liquid on a copper substrate, dried in

https://doi.org/10.1021/acsnano.4c09903
ACS Nano 2025, 19, 3185−3196

a vacuum under an Ar environment, and exposed to ion-irradiation for charge neutralization, followed by a 5 min Ar^+ sputtering to remove the surface and clean any probable contaminants during sample preparation. CasaXPS software was used for the XPS data analysis and peak fitting.

The samples for transmission electron microscopy (TEM) studies were prepared from the fresh supernatant after delamination and centrifugation, and just extra ethanol was added to dilute the supernatant. The colloidal dispersion of 2D-Ta_2Se_2C was then drop-cast onto a TEM copper grid. A multimode atomic force microscope (Bruker Dimension ICON, USA) was used to image the single sheets and measure their thickness. The atomic force microscopy (AFM) sample was prepared by spray-coating DI water-diluted 2D-Ta_2Se_2C colloidal dispersion after exfoliation onto an Ar plasma-cleaned Si substrate. The AFM tip (PPP-NCHR-10, NANOSENSORS) operated under tapping mode to collect the AFM image.

The electrical conductivity of the samples was measured using a ST2253 digital four-probe resistivity meter.

Performance for HER. The electrochemical activities of multilayer and delaminated Ta_2Se_2C were investigated using standard three-electrode cells. Electrodes of drop-cast samples on a rotating disk of glassy carbon (RDGC) were used as the working electrodes. Platinum wire and $Hg/HgSO_4$ in saturated KCl were used as counter and reference electrodes, respectively. An aqueous 0.5 M H_2SO_4 solution was used as the electrolyte. Before electrochemical measurements were started, the electrolyte was bubbled with H_2 or Ar gas for at least 30 min and kept bubbling during measurements. The cell was connected to a BioLogic Potentiostat-Galvanostat equipped with EC-lab software.

To prepare the working electrodes, 10 mg of each sample was added to a solution containing 100 μL of DI water, 90 μL of ethanol, and 10 μL of Nafion solution (alcohol-based, 1000 EW at 5 wt %, ION POWER). The slurry was sonicated for 15 min at 25 °C. Then, 3.3 μL of the slurry was dropped on the surface of a mirror-like polished RDGC with a 3 mm diameter and dried under ambient conditions for about 30 min (loading ~2.3 mg·cm^{-2}).

To investigate the electrochemical performance, first, the OCP of the cell was measured, and 20 CVs were performed with a potential window of OCP ±50 mV at a scan rate of 20 mV·s^{-1}. LSV was conducted at a scan rate of 5 mV·s^{-1} in a potential window of 0 to −0.8 V vs RHE. The PEIS was performed at a range of 100 kHz to 100 mHz with a sinus amplitude of 10 mV to appraise the reaction kinetics and to measure the charge transfer resistance (R_{ct}) at the electrode/electrolyte interface,[68] and all the potential values were *iR*-corrected and reported versus RHE according to R_{ct} obtained from the PEIS measurements. The current values were converted to the geometric current density. The Tafel polarization slope was calculated from the LSV data. CVs at different scan rates were recorded, and from that, the C_{dl} of each material was extracted in the nonfaradaic region, and from that, the ECSA was calculated.[69]

Computational Method. All calculations in this work were performed applying DFT with the Perdew, Burke, and Ernzerhof generalized gradient functional (GGA-PBE)[70] with the Tkatchenko–Scheffler method[71] for van der Waals interactions. A 7 × 1 × 1 *k*-point mesh was used with a 400 eV cutoff energy. All calculations were done using the Vienna Ab initio Simulation Package (VASP),[72] and structures were visualized using Visual Molecular Dynamics.[72]

In this work, a 3 × 3 unit cell was used containing nine M_2S_2C or M_2Se_2C formula units (M = Nb or Ta). Roughly 12 Å of vacuum was inserted in the *y*-direction to form an edge and the *z*-direction to separate the layers. All atoms were relaxed during optimization. The Gibbs free energy (300 K) of hydrogen adsorption was defined as

$$\Delta G_{H^*} = G_{TMCC\text{-}H} - G_{TMCC} - 1/2G_{H2}$$

where $G_{TMCC\text{-}H}$ is the free energy of a TMCC with an adsorbed H atom, G_{TMCC} is the free energy of the clean TMCC, and G_{H2} is the free energy of the hydrogen molecule in the gas phase. The free energy *G* was calculated as

$$G = E + ZPE - TS$$

where *E* is the electronic energy, ZPE is the zero-point energy, *T* is the temperature, and *S* is the entropy.

ASSOCIATED CONTENT

Supporting Information

The Supporting Information is available free of charge at https://pubs.acs.org/doi/10.1021/acsnano.4c09903.

Further details on the synthesis, characterization, and additional electrochemical results for Ta_2Se_2C and $TaSe_2$ and calculations for ECSA, theoretical specific surface area, and TOF for 2D Ta_2Se_2C (PDF)

AUTHOR INFORMATION

Corresponding Author

Michael Naguib − *Department of Physics and Engineering Physics, Tulane University, New Orleans, Louisiana 70118, United States;* orcid.org/0000-0002-4952-9023; Email: naguib@tulane.edu

Authors

Elham Loni − *Department of Physics and Engineering Physics, Tulane University, New Orleans, Louisiana 70118, United States*

Ahmad Majed − *Department of Physics and Engineering Physics, Tulane University, New Orleans, Louisiana 70118, United States*

Shengjie Zhang − *Department of Chemical and Biomolecular Engineering, Tulane University, New Orleans, Louisiana 70118, United States*

Hari H. S. Thangavelu − *Department of Physics, Chemistry and Biology, Linköping University, Linköping SE-581 83, Sweden*

Chaochao Dun − *The Molecular Foundry, Lawrence Berkeley National Laboratory, Berkeley, California 94720, United States;* orcid.org/0000-0002-3215-6478

Anika Tabassum − *Department of Physics and Engineering Physics, Tulane University, New Orleans, Louisiana 70118, United States*

Karamullah Eisawi − *Department of Physics and Engineering Physics, Tulane University, New Orleans, Louisiana 70118, United States;* orcid.org/0000-0002-9031-4809

Jeffrey J. Urban − *The Molecular Foundry, Lawrence Berkeley National Laboratory, Berkeley, California 94720, United States;* orcid.org/0000-0003-4909-2869

Per O. Å. Persson − *Department of Physics, Chemistry and Biology, Linköping University, Linköping SE-581 83, Sweden;* orcid.org/0000-0001-9140-6724

Matthew M. Montemore − *Department of Chemical and Biomolecular Engineering, Tulane University, New Orleans, Louisiana 70118, United States;* orcid.org/0000-0002-4157-1745

Complete contact information is available at: https://pubs.acs.org/10.1021/acsnano.4c09903

Author Contributions

The manuscript was written through the contributions of all authors. All authors have given approval to the final version of the manuscript.

Notes

The authors declare no competing financial interest.

https://doi.org/10.1021/acsnano.4c09903
ACS Nano 2025, 19, 3185−3196

ACKNOWLEDGMENTS

This work was supported by the National Science Foundation under grant no. DMR-2048164. The computational work was supported by Tulane University and the National Science Foundation through grant no. CHE-2154952. The authors acknowledge the Swedish Research Council (VR) and the Swedish Foundation for Strategic Research (SSF) for access to ARTEMI, the Swedish National Infrastructure in Advanced Electron Microscopy (nos. 2021-00171 and RIF21-0026). POÅP also acknowledges VR for project funding (2021-04499). Work at the Molecular Foundry was supported by the Office of Science, Office of Basic Energy Sciences, of the U.S. Department of Energy under Contract No. DE-AC02-05CH11231.

REFERENCES

(1) Manzeli, S.; Ovchinnikov, D.; Pasquier, D.; Yazyev, O. V.; Kis, A. 2D Transition Metal Dichalcogenides. *Nat. Rev. Mater.* **2017**, *2*, 17033−17115.
(2) Liu, F.; Zhou, J.; Zhu, C.; Liu, Z. Electric Field Effect in Two-Dimensional Transition Metal Dichalcogenides. *Adv. Funct. Mater.* **2017**, *27*, 1602404.
(3) Wang, Q. H.; Kalantar-Zadeh, K.; Kis, A.; Coleman, J. N.; Strano, M. S. Electronics and Optoelectronics of Two-Dimensional Transition Metal Dichalcogenides. *Nat. Nanotechnol.* **2012**, *7*, 699−712.
(4) Yun, Q.; Li, L.; Hu, Z.; Lu, Q.; Chen, B.; Zhang, H. Layered Transition Metal Dichalcogenide-Based Nanomaterials for Electrochemical Energy Storage. *Adv. Mater.* **2020**, *32*, 1903826.
(5) Fu, Q.; Han, J.; Wang, X.; Xu, P.; Yao, T.; Zhong, J.; Zhong, W.; Liu, S.; Gao, T.; Zhang, Z.; Xu, L.; et al. 2D Transition Metal Dichalcogenides: Design, Modulation, and Challenges in Electrocatalysis. *Adv. Mater.* **2021**, *33*, 1907818.
(6) Duan, X.; Xu, J.; Wei, Z.; Ma, J.; Guo, S.; Liu, H.; Dou, S. Atomically Thin Transition-Metal Dichalcogenides for Electrocatalysis and Energy Storage. *Small Methods* **2017**, *1*, 1700156.
(7) Noh, S. H.; Hwang, J.; Kang, J.; Seo, M. H.; Choi, D.; Han, B. Tuning The Catalytic Activity Of Heterogeneous Two-Dimensional Transition Metal Dichalcogenides for Hydrogen Evolution. *J. Mater. Chem. A* **2018**, *6*, 20005−20014.
(8) Yang, R.; Fan, Y.; Zhang, Y.; Mei, L.; Zhu, R.; Qin, J.; Hu, J.; Chen, Z.; Hau Ng, Y.; Voiry, D.; Li, S.; et al. 2D Transition Metal Dichalcogenides for Photocatalysis. *Angew. Chem.* **2023**, *135*, No. e202218016.
(9) Lukowski, M. A.; Daniel, A. S.; Meng, F.; Forticaux, A.; Li, L.; Jin, S. Enhanced Hydrogen Evolution Catalysis from Chemically Exfoliated Metallic MoS_2 Nanosheets. *J. Am. Chem. Soc.* **2013**, *135*, 10274−10277.
(10) Voiry, D.; Salehi, M.; Silva, R.; Fujita, T.; Chen, M.; Asefa, T.; Shenoy, V. B.; Eda, G.; Chhowalla, M. Conducting MoS_2 Nanosheets as Catalysts for Hydrogen Evolution Reaction. *Nano Lett.* **2013**, *13*, 6222−6227.
(11) Mondal, A.; Vomiero, A. 2D Transition Metal Dichalcogenides-Based Electrocatalysts for Hydrogen Evolution Reaction. *Adv. Funct. Mater.* **2022**, *32*, 2208994.
(12) Tsai, C.; Chan, K.; Nørskov, J. K.; Abild-Pedersen, F. Theoretical Insights into The Hydrogen Evolution Activity of Layered Transition Metal Dichalcogenides. *Surf. Sci.* **2015**, *640*, 133−140.
(13) Gan, X.; Lee, L. Y. S.; Wong, K. Y.; Lo, T. W.; Ho, K. H.; Lei, D. Y.; Zhao, H. 2H/1T Phase Transition of Multilayer MoS_2 by Electrochemical Incorporation of S Vacancies. *ACS Appl. Energy Mater.* **2018**, *1*, 4754−4765.
(14) Zhang, Y.; Wang, J.; Nong, H.; He, L.; Li, S.; Wei, Q.; Wu, Q.; Liu, B. Reducing Atomic Defects in 2D Transition Metal Dichalcogenides. *Adv. Funct. Mater.* **2024**, *34*, 2410402.
(15) Naguib, M.; Kurtoglu, M.; Presser, V.; Lu, J.; Niu, J.; Heon, M.; Hultman, L.; Gogotsi, Y.; Barsoum, M. W. Two-Dimensional Nanocrystals Produced by Exfoliation of Ti_3AlC_2. *Adv. Mater.* **2011**, *23*, 4248−4253.
(16) Majed, A.; Kothakonda, M.; Wang, F.; Tseng, E. N.; Prenger, K.; Zhang, X.; Persson, P. O.; Wei, J.; Sun, J.; Naguib, M. Transition Metal Carbo-Chalcogenide "TMCC:" A New Family of 2D Materials. *Adv. Mater.* **2022**, *34*, 2200574.
(17) Beckmann, O. H.; Boller, H.; Nowotny, H. Die Kristallstrukturen Von Ta_2S_2C Und Ti_4S_5 ($Ti_{0.81}S$). *Monatsh. Chem.* **1970**, *101*, 945−955.
(18) Boller, H.; Hiebl, K. Quaternary Pseudo-Intercalation Phases $T_x[Nb_2S_2C]$(Ti, V, Cr, Mn, Fe, Co, Ni, Cu) and Metastable Nb_2S_2C Formed by Topochemical Synthesis. *J. Alloys Compd.* **1992**, *183*, 438−443.
(19) Sakamaki, K.; Wada, H.; Nozaki, H.; Ōnuki, Y.; Kawai, M. Topochemical Formation of Van Der Waals Type Niobium Carbosulfide 1T-Nb_2S_2C. *J. Alloys Compd.* **2002**, *339*, 283−292.
(20) Jing, Y.; Liu, J.; Zhou, Z.; Zhang, J.; Li, Y. Metallic Nb_2S_2C Monolayer: A Promising Two-Dimensional Anode Material for Metal-Ion Batteries. *J. Phys. Chem. C* **2019**, *123*, 26803−26811.
(21) Music, D.; Sun, Z.; Schneider, J. M. Ab Initio Study Of Nb_2SC and Nb_2S_2C: Differences in Coupling Between The S And Nb−C Layers. *Solid State Commun.* **2006**, *137*, 306−309.
(22) Baaziz, H.; Ghellab, T.; Charifi, Z.; Güler, M.; Uğur, Ş.; Güler, E.; Genç, A. E.; Uğur, G. Full Potential Theoretical Investigations For Electronic, Optical, Mechanical, Elastic and Anisotropic Properties of X_2Se_2C (X= Ta, Nb) Compounds. *Eur. Phys. J. B* **2023**, *96*, 55.
(23) Hug, G. Electronic Structures of and Composition Gaps Among The Ternary Carbides Ti_2MC. *Phys. Rev. B:Condens. Matter Mater. Phys.* **2006**, *74*, 184113.
(24) Hu, T.; Wang, M.; Cai, C.; Cheng, R.; Wang, J.; Guo, C.; Ren, L.; Li, C. M.; Wang, X. Van der Waals Transition Metal Carbo-Chalcogenides: Theoretical Screening and Charge Storage. *Small* **2024**, *20*, 2402076.
(25) Zhang, Y.; Xu, M.; Zeng, Q.; Hao, J.; Li, Y. Effect of Nb-X Ionic Bonding on The Superconductivity of The Two-Dimensional Nb_2S_XC (X= O, S, Se, F, Cl, and Br). *Mater. Today Electron.* **2023**, *5*, 100053.
(26) Chen, K.; Ye, Q.; Zhou, J.; Shen, L.; Xue, J.; Huang, Q. Synthesis of Ti_2SC Phase Using Iron Disulfide or Iron Sulfide Post-Treated with Acid. *J. Am. Ceram. Soc.* **2015**, *98*, 1074−1079.
(27) Naguib, M.; Mashtalir, O.; Carle, J.; Presser, V.; Lu, J.; Hultman, L.; Gogotsi, Y.; Barsoum, M. W. Two-Dimensional Transition Metal Carbides. *ACS Nano* **2012**, *6*, 1322−1331.
(28) Yang, R.; et al. High-Yield Production of Mono-or Few-Layer Transition Metal Dichalcogenide Nanosheets by An Electrochemical Lithium Ion Intercalation-Based Exfoliation Method. *Nat. Protoc.* **2022**, *17*, 358−377.
(29) Muckley, E. S.; Naguib, M.; Wang, H. W.; Vlcek, L.; Osti, N. C.; Sacci, R. L.; Sang, X.; Unocic, R. R.; Xie, Y.; Tyagi, M.; Mamontov, E.; et al. Multimodality of Structural, Electrical, and Gravimetric Responses of Intercalated MXenes to Water. *ACS Nano* **2017**, *11*, 11118−11126.
(30) Mashtalir, O.; Naguib, M.; Mochalin, V. N.; Dall'Agnese, Y.; Heon, M.; Barsoum, M. W.; Gogotsi, Y. Intercalation and Delamination of Layered Carbides and Carbonitrides. *Nat. Commun.* **2013**, *4*, 1716.
(31) Saxena, S.; Chaudhary, R. P.; Shukla, S. Stanene: Atomically Thick Free-Standing Layer of 2D Hexagonal Tin. *Sci. Rep.* **2016**, *6*, 31073.
(32) Liu, H.; Lei, W.; Tong, Z.; Li, X.; Wu, Z.; Jia, Q.; Zhang, S.; Zhang, H. Defect Engineering of 2D Materials For Electrochemical Energy Storage. *Adv. Mater. Interfaces* **2020**, *7*, 2000494.
(33) Sun, T.; Zhang, G.; Xu, D.; Lian, X.; Li, H.; Chen, W.; Su, C. Defect Chemistry in 2D Materials for Electrocatalysis. *Mater. Today Energy* **2019**, *12*, 215−238.
(34) Wang, X.; Zhang, Y.; Wu, J.; Zhang, Z.; Liao, Q.; Kang, Z.; Zhang, Y. Single-Atom Engineering To Ignite 2D Transition Metal

https://doi.org/10.1021/acsnano.4c09903
ACS Nano 2025, 19, 3185−3196

Dichalcogenide Based Catalysis: Fundamentals, Progress, and Beyond. *Chem. Rev.* **2022**, *122*, 1273−1348.
(35) Zhao, S.; Chen, G.; Zhou, G.; Yin, L. C.; Veder, J. P.; Johannessen, B.; Saunders, M.; Yang, S. Z.; De Marco, R.; Liu, C.; Jiang, S. P. A Universal Seeding Strategy To Synthesize Single-Atom Catalysts on 2D Materials for Electrocatalytic Applications. *Adv. Funct. Mater.* **2020**, *30*, 1906157.
(36) Yang, W.; Cheng, Y.; Jiang, M.; Jiang, S.; Liu, R.; Lu, J.; Du, L.; Li, P.; Wang, C. Design and Fabrication of An Ultra-Sensitive Ta_2C MXene/Au-Coated Tilted Grating Sensor. *Sens. Actuators, B* **2022**, *369*, 132391.
(37) Ge, Y.; Wang, F.; Yang, Y.; Xu, Y.; Ye, Y.; Cai, Y.; Zhang, Q.; Cai, S.; Jiang, D.; Liu, X.; Liedberg, B.; et al. Atomically Thin $TaSe_2$ Film as A High-Performance Substrate for Surface-Enhanced Raman Scattering. *Small* **2022**, *18*, 2107027.
(38) Deng, Y.; Lai, Y.; Zhao, X.; Wang, X.; Zhu, C.; Huang, K.; Zhu, C.; Zhou, J.; Zeng, Q.; Duan, R.; Fu, Q.; et al. Controlled Growth of 3R Phase Tantalum Diselenide and Its Enhanced Superconductivity. *J. Am. Chem. Soc.* **2020**, *142*, 2948−2955.
(39) Moo, J. G. S.; Awaludin, Z.; Okajima, T.; Ohsaka, T. An XPS Depth-Profile Study on Electrochemically Deposited TaO_x. *J. Solid State Electrochem.* **2013**, *17*, 3115−3123.
(40) Kerrec, O.; Devilliers, D.; Groult, H.; Marcus, P. Study of Dry and Electrogenerated Ta_2O_5 and $Ta/Ta_2O_5/Pt$ Structures by XPS. *Mater. Sci. Eng., B* **1998**, *55*, 134−142.
(41) Halim, J.; Cook, K. M.; Naguib, M.; Eklund, P.; Gogotsi, Y.; Rosen, J.; Barsoum, M. W. X-Ray Photoelectron Spectroscopy of Select Multi-Layered Transition Metal Carbides (MXenes). *Appl. Surf. Sci.* **2016**, *362*, 406−417.
(42) Näslund, L.-Å.; Persson, P. O.; Rosen, J. X-Ray Photoelectron Spectroscopy of Ti_3AlC_2, $Ti_3C_2T_z$, And TiC Provides Evidence for The Electrostatic Interaction Between Laminated Layers in MAX-Phase Materials. *J. Phys. Chem. C* **2020**, *124*, 27732−27742.
(43) Shang, X.; Chen, W.; Jiang, Z. J.; Song, C.; Jiang, Z. In Situ Growth of SeO_x Films on The Surface Of Ni−Fe−Selenide Nanosheets as Highly Active and Stable Electrocatalysts for The Oxygen Evolution Reaction. *Mater. Adv.* **2022**, *3*, 2546−2557.
(44) Jang, Y.; Lee, S. Revealing the Importance of SeOx Formation in Nickel-Iron Selenides for Improving Oxygen Evolution Activity. *SSRN* **2024**, DOI: 10.2139/ssrn.4836666.
(45) Biesinger, M. C. Accessing The Robustness of Adventitious Carbon for Charge Referencing (Correction) Purposes in XPS Analysis: Insights from A Multi-User Facility Data Review. *Appl. Surf. Sci.* **2022**, *597*, 153681.
(46) Khanal, V.; Irani, R.; Fiechter, S.; Abdi, F. F.; Subramanian, V. R. The Photoelectrochemical and Photocatalytic Properties of Tantalum Oxide Ond Tantalum Nitride. *J. Electrochem. Soc.* **2019**, *166*, H3294.
(47) Pai, Y. H.; Chou, C. C.; Shieu, F. S. Preparation and Optical Properties of Ta_2O_{5-X} Thin Films. *Mater. Chem. Phys.* **2008**, *107*, 524−527.
(48) Kim, Y. J.; et al. Tailoring Two-Dimensional Matter Using Strong Light-Matter Interactions. *Nano Lett.* **2023**, *23*, 3645−3652.
(49) Pachuta, K.; Pentzer, E.; Sehirlioglu, A. Evaluating the Chemical Exfoliation of Lithium Cobalt Oxide Using UV-vis Spectroscopy. *Nanoscale Adv.* **2020**, *2*, 5362−5374.
(50) Backes, C.; Higgins, T. M.; Kelly, A.; Boland, C.; Harvey, A.; Hanlon, D.; Coleman, J. N. Guidelines For Exfoliation, Characterization and Processing of Layered Materials Produced by Liquid Exfoliation. *Chem. Mater.* **2017**, *29*, 243−255.
(51) Jana, M. K.; Rao, C. Two-Dimensional Inorganic Analogues of Graphene: Transition Metal Dichalcogenides. Philosophical Transactions of The Royal Society A: Mathematical. *Phys. Eng. Sci.* **2016**, *374*, 20150318.
(52) Voiry, D.; Fullon, R.; Yang, J.; de Carvalho Castro eSilva, C.; Kappera, R.; Bozkurt, I.; Kaplan, D.; Lagos, M. J.; Batson, P. E.; Gupta, G.; Mohite, A. D.; et al. The Role of Electronic Coupling Between Substrate and 2D MoS_2 Nanosheets in Electrocatalytic Production of Hydrogen. *Nat. Mater.* **2016**, *15*, 1003−1009.
(53) Hasan, M. M.; Allam, N. K. An Alternative, Low-Dissolution Counter Electrode to Prevent Deceptive Enhancement of HER Overpotential. *Sci. Rep.* **2022**, *12*, 9368.
(54) Chen, R.; Yang, C.; Cai, W.; Wang, H. Y.; Miao, J.; Zhang, L.; Chen, S.; Liu, B. Use of platinum as the counter electrode to study the activity of nonprecious metal catalysts for the hydrogen evolution reaction. *ACS Energy Lett.* **2017**, *2*, 1070−1075.
(55) Thangasamy, P.; Oh, S.; Nam, S.; Oh, I. K. Rose-Like MoS_2 Nanostructures with A Large Interlayer Spacing of 9.9 Å and Exfoliated WS_2 Nanosheets Supported on Carbon Nanotubes for Hydrogen Evolution Reaction. *Carbon* **2020**, *158*, 216−225.
(56) Chen, H.; Si, J.; Lyu, S.; Zhang, T.; Li, Z.; Lei, C.; Lei, L.; Yuan, C.; Yang, B.; Gao, L.; Hou, Y. Highly Effective Electrochemical Exfoliation of Ultrathin Tantalum Disulfide Nanosheets for Energy-Efficient Hydrogen Evolution Electrocatalysis. *ACS Appl. Mater. Interfaces* **2020**, *12*, 24675−24682.
(57) Gao, Y.; Chen, Z.; Zhao, Y.; Yu, W.; Jiang, X.; He, M.; Li, Z.; Ma, T.; Wu, Z.; Wang, L. Facile Synthesis Of MoP-Ru_2P on Porous N, P Co-Doped Carbon for Efficiently Electrocatalytic Hydrogen Evolution Reaction in Full PH Range. *Appl. Catal., B* **2022**, *303*, 120879.
(58) Verma, A.; Dutta, A. Chalcogen Vacancy-Enhanced Electrocatalytic Activity of 2D Janus NbSSe Monolayers for Hydrogen Evolution. *Int. J. Hydrogen Energy* **2024**.
(59) Hu, Z.; Wu, Z.; Han, C.; He, J.; Ni, Z.; Chen, W. Two-Dimensional Transition Metal Dichalcogenides: Interface and Defect Engineering. *Chem. Soc. Rev.* **2018**, *47*, 3100−3128.
(60) Shinagawa, T.; Garcia-Esparza, A. T.; Takanabe, K. Insight on Tafel Slopes from A Microkinetic Analysis of Aqueous Electrocatalysis for Energy Conversion. *Sci. Rep.* **2015**, *5*, 13801.
(61) Wang, M.; Zhang, L.; Huang, M.; Liu, Y.; Zhong, Y.; Pan, J.; Wang, Y.; Zhu, H. Morphology-Controlled Tantalum Diselenide Structures ss Self-Optimizing Hydrogen Evolution Catalysts. *Energy Environ. Mater.* **2020**, *3*, 12−18.
(62) Meyer, S.; Nikiforov, A. V.; Petrushina, I. M.; Köhler, K.; Christensen, E.; Jensen, J. O.; Bjerrum, N. J. Transition Metal Carbides (WC, Mo_2C, TaC, NbC) as Potential Electrocatalysts for The Hydrogen Evolution Reaction (HER) at Medium Temperatures. *Int. J. Hydrogen Energy* **2015**, *40*, 2905−2911.
(63) Singh, B.; Gawande, M. B.; Kute, A. D.; Varma, R. S.; Fornasiero, P.; McNeice, P.; Jagadeesh, R. V.; Beller, M.; Zbořil, R. Single-Atom (Iron-Based) Catalysts: Synthesis and Applications. *Chem. Rev.* **2021**, *121*, 13620−13697.
(64) Xue, Y.; Huang, B.; Yi, Y.; Guo, Y.; Zuo, Z.; Li, Y.; Jia, Z.; Liu, H.; Li, Y. Anchoring Zero Valence Single Atoms of Nickel And Iron on Graphdiyne For Hydrogen Evolution. *Nat. Commun.* **2018**, *9*, 1460.
(65) Stratton, S. M.; Zhang, S.; Montemore, M. M. Addressing complexity in catalyst design: From Volcanos and Scaling to More Sophisticated Design Strategies. *Surf. Sci. Rep.* **2023**, *78*, 100597.
(66) Ramezani, H. R.; Şaşıoğlu, E.; Hadipour, H.; Soleimani, H. R.; Friedrich, C.; Blügel, S.; Mertig, I. Nonconventional Screening of Coulomb Interaction in Two-Dimensional Semiconductors and Metals: A Comprehensive Constrained Random Phase Approximation Study of MX_2 (M= Mo, W, Nb, Ta; X= S, Se, Te). *Phys. Rev. B* **2024**, *109*, 125108.
(67) Li, M.; Li, T.; Jing, Y. Nb_2S_2C Monolayers With Transition Metal Atoms Embedded at The S Vacancy Are Promising Single-Atom Catalysts for CO Oxidation. *ACS Omega* **2023**, *8*, 31051−31059.
(68) Durst, J.; Simon, C.; Siebel, A.; Rheinländer, P. J.; Schuler, T.; Hanzlik, M.; Herranz, J.; Hasché, F.; Gasteiger, H. A. Hydrogen Oxidation and Evolution Reaction (HOR/HER) on Pt Electrodes in Acid vs. Alkaline Electrolytes: Mechanism, Activity and Particle Size Effects. *ECS Trans.* **2014**, *64*, 1069.
(69) Cossar, E.; Houache, M. S.; Zhang, Z.; Baranova, E. A. Comparison of Electrochemical Active Surface Area Methods for Various Nickel Nanostructures. *J. Electroanal. Chem.* **2020**, *870*, 114246.

https://doi.org/10.1021/acsnano.4c09903
ACS Nano 2025, 19, 3185−3196

(70) Perdew, J. P.; Burke, K.; Ernzerhof, M. Generalized Gradient Approximation Made Simple. *Phys. Rev. Lett.* **1996**, *77*, 3865.
(71) Tkatchenko, A.; Scheffler, M. Accurate Molecular Van Der Waals Interactions from Ground-State Electron Density and Free-Atom Reference Data. *Phys. Rev. Lett.* **2009**, *102*, 073005.
(72) Kresse, G.; Furthmüller, J. Efficiency of Ab-Initio Total Energy Calculations for Metals and Semiconductors Using A Plane-Wave Basis Set. *Comput. Mater. Sci.* **1996**, *6*, 15−50.

https://doi.org/10.1021/acsnano.4c09903
ACS Nano 2025, 19, 3185−3196